Uncondensed Graphitic Carbon Nitride on Reduced Graphene Oxide for Oxygen Sensing *via* a Photoredox Mechanism

James E. Ellis[1], Dan C. Sorescu[2,3], Seth C. Burkert[1], David L. White[1], and Alexander Star[1]*

1. Department of Chemistry, University of Pittsburgh, Pittsburgh, Pennsylvania 15260, United States

2. United States Department of Energy, National Energy Technology Laboratory, Pittsburgh, Pennsylvania 15236, United States

3. Department of Chemical and Petroleum Engineering, University of Pittsburgh, Pittsburgh, PA 15261, U.S.A.

KEYWORDS: Carbon nitride, graphene, photoredox, charge transfer, oxygen sensing, chemiresistor

ABSTRACT: Melon, a polymeric, uncondensed graphitic carbon nitride with a two-dimensional structure has been coupled with reduced graphene oxide (rGO) to create an oxygen chemiresistor sensor that is active under UV photoactivation. Oxygen gas is an important sensor target in a variety of areas including industrial safety, combustion process monitoring, as well as environmental and biomedical fields. Due to the intimate electrical interface formed between melon and rGO, charge transfer of photoexcited electrons occurs between the two materials when under UV (λ=365 nm) irradiation. A photoredox mechanism wherein oxygen is reduced on the rGO surface provides the basis for sensing oxygen gas in the concentration range between 300-10,000 ppm. The sensor response was found to be logarithmically proportional to oxygen gas concentration. DFT calculations of a melon-oxidized graphene composite found that slight protonation of melon leads to charge accumulation on the rGO layer and a corresponding charge depletion on the melon layer. This work provides an example of a metal-free system for solid-gas interface sensing *via* a photoredox mechanism.

1. INTRODUCTION

The ability to detect and quantify the concentration of a specific target gas is an important resource for a variety of fields including medical, industry, and security. In particular, molecular oxygen is a target of interest due to its ubiquity in the environment, in diverse industrial and mechanical processes, and in biological systems. For example, oxygen sensors have been deployed in automobiles and other combustion systems to determine the combustion efficiency, since inefficient combustion is directly related with harmful gas emissions.[1-2] Alternatively, dissolved oxygen concentration in biological systems is an important physiological factor that would be beneficial to sense. For example, hypoxia in tissue cells has been found to correlate with an acceleration of disease progression,[3] including tumor growth.[4] For this reason, nanoscale sensors that can map the oxygen concentration in tissues have been pursued.[5] These examples illustrate the wide-ranging condition requirements (*e.g.,* gas vs. solution; high vs. low pressure, *etc.*) of oxygen sensing applications that drive the development of novel sensing materials and call for an understanding and optimization of their associated working mechanisms.

The research area of gas sensor development, including oxygen sensors, has benefitted from and grown alongside the rise of nanomaterials and of nano-characterization techniques.[6-7] For example, graphene-based materials have shown excellent sensing performance at room temperature to a wide-range of different gases/vapors.[8] In addition, sensor material research has borrowed and adapted many findings from the heterogeneous catalysis field. Common heterogeneous catalyst materials, *e.g.,* metal nanoparticles and metal oxides, have shown excellent sensor properties when coupled with good transducer materials like carbon nanotubes or graphene.[9-11] Catalytic materials provide the receptor function by adsorbing and reacting with certain analytes, while changes in the local chemical environment and minute charge transfers are able to effect observable changes in a carbon nanomaterial's electrical properties due to its large charge carrier mobility and high surface area to volume ratio.[12] Maximizing receptor/transducer interface and choosing receptors that have complementary work functions with the transducer are important strategies for improving sensor sensitivity.

Semiconductor photocatalysts are a class of heterogeneous catalysts that utilize photo-generated electron-hole pairs for photoredox catalysis.[13-14] One such photocatalyst, "graphitic" carbon nitride, is a metal-free semiconductor that has a planar, sheet-like morphology similar to graphene.[15-16] Carbon nitride's bandgap (2.7 eV) is ideal due to its ability to be photoexcited by visible light, and has the proper band structure to catalyze multiple redox reactions;[17] it has shown activity toward water splitting,[18-19] H_2O_2 activation,[20] oxygen reduction reaction (ORR),[21-24] and CO_2 reduction.[24-26] Graphitic carbon nitride is produced by thermally polymerizing cyanamide, dicyandiamide, or melamine at temperatures ranging from 500-600^{o}C. Depending on the precursor and synthetic parameters, the resulting structure can be composed of heptazine[27] or triazine[28] units with different degrees of condensation (condensed-C_3N_4; uncondensed-$C_6N_9H_3$).

The uncondensed form of graphitic carbon nitride, known as melon, was initially speculated to be a linear polymer of heptazine units connected by secondary amine linkages.[29] Structural characterization of melon has found that hydrogen bonding and the presence of π-stacking between polymer units results in its graphitic-like morphology.[30] The weak interplanar

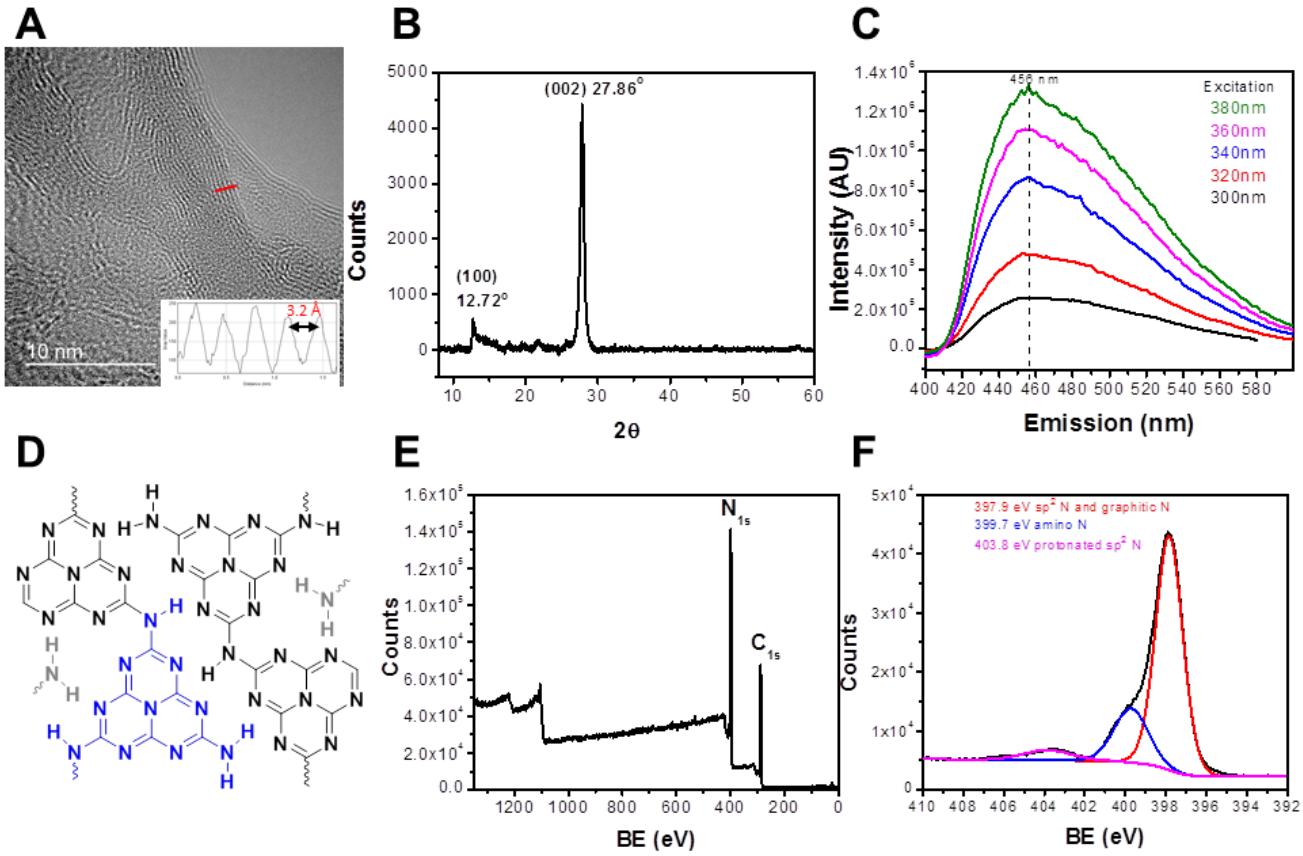

Figure 1. Characterization of synthesized graphitic carbon nitride. (A) HRTEM of exfoliated carbon nitride nanosheets. Inset: Gray scale plot profile of HRTEM cross-section (red line). Peak-to-peak distance (3.2 Å) shows lattice spacing of uncondensed carbon nitride. (B) XRD of as-synthesized carbon nitride material. (C) Fluorescence spectra of as-synthesized carbon nitride powder at different excitation wavelengths (300, 320, 340, 360, and 380 nm). (D) Unit cell of uncondensed graphitic carbon nitride with heptazine monomer (gh-$C_6N_9H_3$). (E) Survey scan of as-synthesized carbon nitride material exhibits N_{1s} peak (60 atomic %) and C_{1s} peak (40 atomic %). H_{1s} cannot be detected with XPS. (F) High-resolution scan of N_{1s} peak shows three deconvolved peaks: protonated sp^2 N (403.8 eV), sp^3 N (399.7 eV), and sp^2 N (397.9 eV). The sp^3 to sp^2 N ratio is ~2:7, which matches the unit cell N ratio of the corresponding species.

interactions existent between sheets allow exfoliation of bulk carbon nitride into carbon nitride nanosheets[19] or quantum dots.[31] Both of these derivative carbon nitride nanomaterials have properties differing from bulk carbon nitride and include an increased bandgap, an increase of the specific surface area, improved electron transport ability along the in-plane direction, and increased lifetimes of photoexcited charge carriers due to the quantum confinement effect. Despite these improvements, carbon nitride still suffers from a fast recombination rate, which limits its use as a photocatalyst and other electrochemical applications.[32].

Hybridization of carbon nitride with carbon nanomaterials has been shown to promote fast separation of photoinduced charge carriers, resulting in a slower recombination rate and increased photocatalytic activity. As an electrocatalyst, carbon nitride hybridized with graphene or carbon nanotubes has shown improved catalytic activity versus pristine carbon nitride for the hydrogen evolution reaction (HER)[33-34] and ORR.[35-36] The presence of carbon nanomaterials does not inhibit photoexcitation of carbon nitride. Graphene has been used as a support as well as a cross-linker to prepare effective photodegradation catalysts.[37-38] Kofuji *et al.*[39] have recently shown that carbon nitride on reduced graphene oxide (rGO) can photocatalytically reduce oxygen to hydrogen peroxide, a potential solar fuel, in the presence of water. In the same paper, it was found that photogenerated electrons are transferred to the rGO surface where oxygen is then reduced *via* a two-electron pathway. In this work, we report a carbon nitride/rGO chemiresistor that can monitor the photogenerated charge separation and subsequent oxygen reduction at the solid-gas interface. This chemiresistor can be utilized as an oxygen sensor in humid environments, wherein the electrical response of the sensor is logarithmically proportional to oxygen concentration.

2. EXPERIMENTAL SECTION

3. RESULTS AND DISCUSSION :

3.1 Carbon Nitride Characterization. Characterization of the as-synthesized carbon nitride material was done to determine whether the material was heptazine- or triazine-based, as well as whether it was condensed or uncondensed (Figure 1). High resolution transmission electron microscopy (HRTEM) of the synthesized carbon nitride material shows a lattice spacing of 3.2 Å (Figure 1A). Powder X-ray diffraction (PXRD) of the as-synthesized material displayed a pattern indicative of layered, graphitic-like sheets (Figure 1B). Since melamine is an intermediate of "graphitic" carbon nitride synthesis, the absence of melamine peaks indicates that reaction went to full completion. The calculated d-spacing of the material is 3.2 Å matches the d-spacing for uncondensed, heptazine-based, graphitic carbon nitride (gh-$C_6N_9H_3$).[30] Bragg's law (eq. 1) was used to derive the d-spacing from the powder X-ray diffraction (PXRD) where $\theta = 13.9^o$ (2θ of 002 peak / 2), $\lambda = 1.54$ Å (wavelength of x-ray source), and n = 1.

$$2dsin\theta = n\lambda \qquad \text{(eq. 1)}$$

Triazine-based graphitic-carbon nitride and condensed carbon nitride (g-C_3N_4) have larger d-spacings of 3.3-3.4 Å.[28, 40-41] The fluorescence emission of the as-synthesized material was measured in the range (300-380 nm)

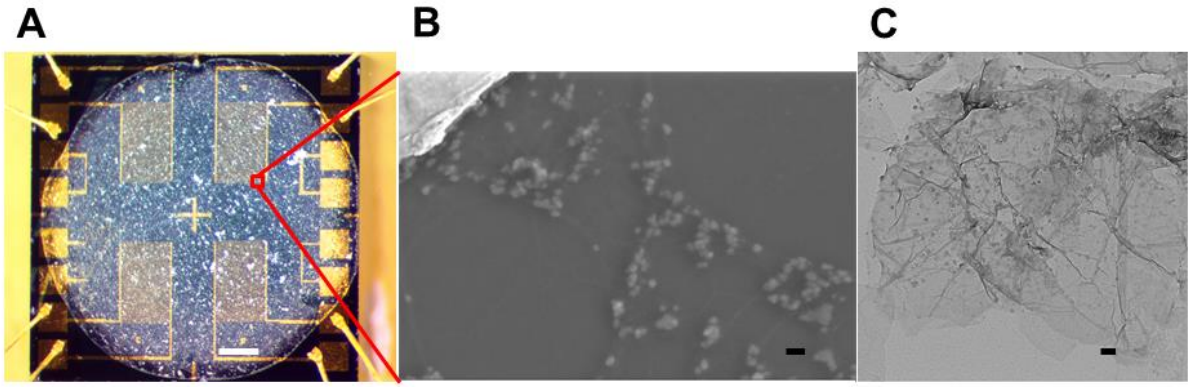

Figure 2. Sensing with carbon nitride/rGO. (A) Optical image of carbon nitride/rGO sensor chip. Scale bar = 250 μm (B) SEM image of rGO decorated with carbon nitride nanosheets between two Au electrodes. (C) TEM of carbon nitride-decorated rGO. The indicated scale bars for (B) and (C) correspond to 100 nm.

of long-wave UV excitation wavelengths (Figure 1C). The emission peak is centered at 456 nm (2.72 eV) for each excitation wavelength, which corresponds well with the bandgap for pristine gh-$C_6N_9H_3$ (referred to as melon in cited reference).[42] The bandgap size of gh-$C_6N_9H_3$ is unique for non-metal materials since it is wide enough to photocatalyze numerous redox pairs, yet narrow enough to absorb visible light. Since proximate ^{1}H atoms are necessary for ^{13}C and ^{15}N CP-MAS solid-state NMR, the appearance of solid-state NMR peaks for the as-synthesized carbon nitride material supports the uncondensed structure of the material (Supporting Information Figure S1). The shifts of the peaks match well with previous literature examples.[30]

XPS of the as-synthesized carbon nitride material confirmed the chemical structure of the material by providing the C to N ratio and the ratio of sp^2 N/graphitic N to sp^3 N (N(-H)$_{1-2}$) (Figures 1E, F). Two peaks, C_{1s} and N_{1s}, appear on the low-resolution survey XPS scan. No elemental impurities are detected. The ratio of carbon to nitrogen is 2C:3N (Figure S2A), which is the empirical formula for uncondensed graphitic carbon nitride (C_2N_3H). Condensed graphitic carbon nitride (g-C_3N_4), on the other hand, has a C:N ratio of 3:4. The high-resolution N_{1s} XPS scan of carbon nitride was deconvolved into three peaks: 397.9 eV (pyridinic and graphitic N); 399.7 eV (amino N); and 403.8 eV (protonated pyridinic N). These N_{1s} peak assignments were made using previous literature assignments of N-functionalities on sp^2 carbon.[43-44] The unit cell for gh-$C_6N_9H_3$ (Figure 1D) contains a total of 36 nitrogen atoms, of which 28 N atoms are pyridinic or graphitic, and 8 N atoms are amino (*i.e.* N(-H)$_{1-2}$). This composition (77.78% pyridinic plus graphitic N; 22.22% amino N) is closely matched by the high-resolution N_{1s} XPS peaks in which 78.19% of N atoms are pyridinic (including protonated)/graphitic N and 21.81% are amino N (Figure S2B).

The XPS peak centered at 403.8 eV, which accounts for 2 of the 36 N atoms in the unit cell (Figure 1D), can be explained by protonation of two pyridinic N atoms in the gh-$C_6N_9H_3$ unit cell. There are a total of six sp^2 N sites in the gh-$C_6N_9H_3$ unit cell where protonation can potentially occur (Figure S3). Pels *et al.* observed that positively-charged N species in pyrolyzed coals and chars led to XPS peaks similar to quaternary N peaks in the range of 401-405 eV.[44-45] In the case of carbon nitride, the peak at 404 eV has been attributed to positive charge localization on the heterocycle structure.[46] Protonation of sp^2 N in carbon nitride would lead to positive charge localization within the heptazine unit of the polymer.[47] The effect of protonation on carbon nitride's charge transfer dynamics was investigated with DFT calculations (*vide infra*).

3.2 Carbon nitride/rGO chemiresistor. Sensor devices were prepared by sequentially depositing rGO and exfoliated carbon nitride between interdigitated gold electrodes. rGO sheets used in this work were between 0.5-2 μm wide and contained structural defects such as wrinkles and grain boundaries on the graphitic basal plane (Figure S4). The distance between interdigitated electrodes of the chemiresistor devices are 8 μm, thus requiring the deposition of several overlapping rGO sheets to bridge the electrodes. Effective deposition of rGO sheets between the interdigitated electrodes was tested by taking current-voltage (I-V) curves after the dielectrophoresis (DEP) procedure. A current in the μA range at 1 V was found to correspond to an ideal deposition, since lower currents represent an unreliably low concentration of rGO between the electrodes while higher currents represent an overabundance of rGO sheets resulting in sensor insensitivity.

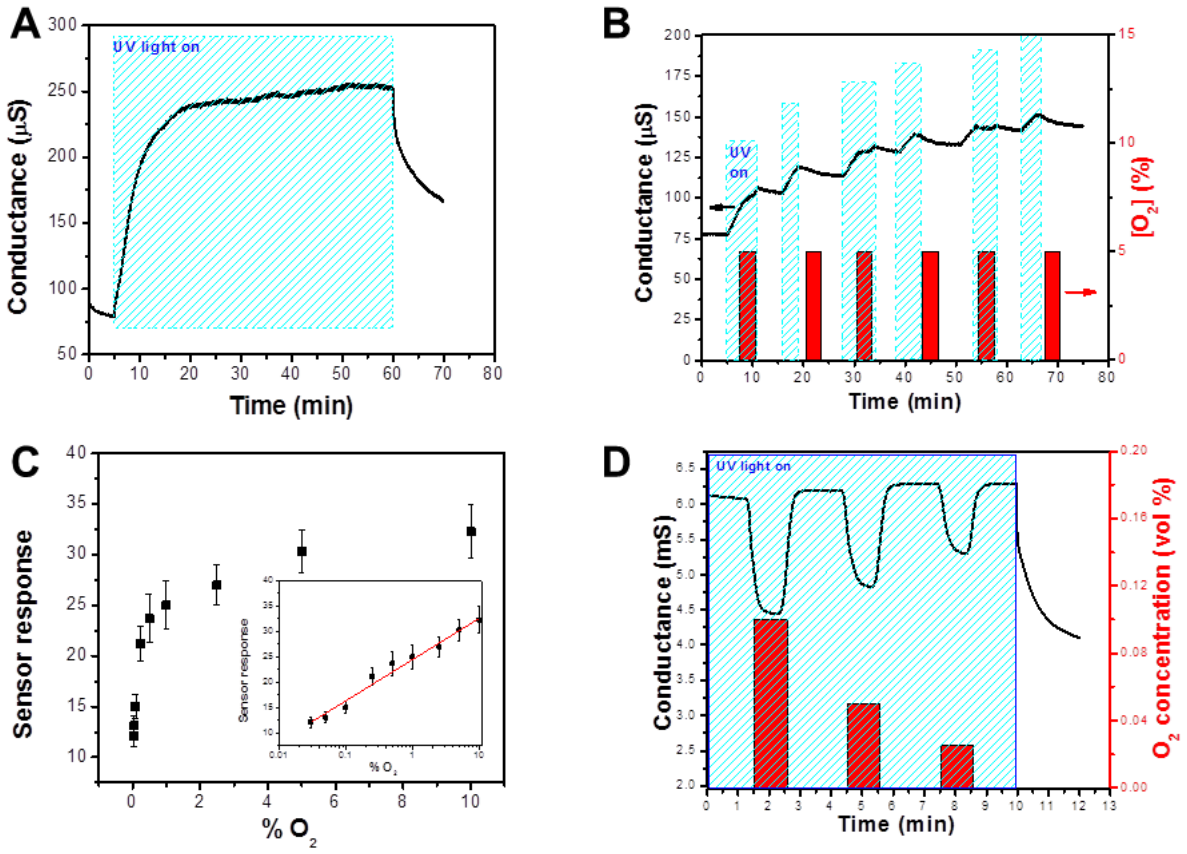

Figure 3. **Conductance measurements of chemiresistor devices.** (A) Carbon nitride/rGO in humid N_2; (B) carbon nitride/rGO with 3 min exposures of O_2 in dry N_2;; (C) sensor response (see eq. 2) vs. O_2 concentration. Inset: X-axis changed to logarithmic scale to illustrate the logarithmic dependence of the sensor response; (D) carbon nitride/rGO chemiresistor in humid N_2 with 1 minute exposures of O_2.

Uniform distribution of carbon nitride nanosheets across the Si sensor chip was achieved with the dropcast procedure (Figure 2A), which provided similar sensing behavior among the four chemiresistor devices. Exfoliation of the carbon nitride material was done with bath sonication of an aqueous dispersion. It was found that an hour of sonication was sufficient to exfoliate 1-3 μm carbon nitride sheets into 10-100 nm nanosheets (Figure S5). The carbon nitride nanosheets were found to deposit on the wrinkles and edges of the rGO sheet (Figure 2B, C). Wrinkles, grain boundaries, and edges of rGO are known to contain a higher concentration of defect sites and oxygen moieties as compared to flat basal plane regions of the rGO sheet.[48-49] The carbon nitride nanosheets can be removed off the rGO with a water wash, thus demonstrating the non-covalent nature of the carbon nitride/rGO interface. Ong *et al.* have shown that electrostatic interaction between the protonated carbon nitride and the oxygen moieties on rGO is the dominant intermolecular force between the two materials.[50]

3.3 Oxygen sensing with carbon nitride/rGO. Carbon nitride/rGO chemiresistor devices were tested in various gas environments with and without UV irradiation. Though carbon nitride can be photoexcited with visible light, longwave UV light (365-390 nm) was used in this work because UV light has a cleaning effect on graphene by removing surface contaminants.[51] When the carbon nitride/rGO chemiresistor was irradiated with UV light in a humid N_2 environment, a sharp increase in electrical conductance was observed (Figure 3A). In the same experiment a saturation point in conductance is reached after 15 minutes of UV irradiation (950 μW/cm^2), which is more than double the initial conductance measured before UV irradiation. UV light is known to photoexcite carbon nitride;[52] therefore, the increase in the chemiresistor's conductance can be explained by photogeneration of charge carriers in the carbon nitride nanosheets and subsequent transfer of charge carriers into the rGO transducer. In a humid nitrogen environment, the carbon nitride/rGO chemiresistor recovers back towards its baseline once UV light is removed. UV irradiation of a bare rGO chemiresistor showed a small decrease in conductance (Figure S6), likely due to UV light's cleaning effect of surface contaminants. Therefore, the two-fold conductance increase of the carbon nitride/rGO chemiresistor under UV light is the result of charge carrier photogeneration in carbon nitride nanosheets. Likewise, the carbon nitride/rGO chemiresistor in dry nitrogen conditions also rose in conductance when irradiated with UV light; however, once the UV light was removed the chemiresistor shows little to no recovery back to baseline (Figure S7). The difference between baseline recovery post-UV light in humid nitrogen versus dry nitrogen indicates that H_2O, or O_2 evolved from H_2O oxidation, is responsible for the baseline recovery.

Exfoliation of graphitic carbon nitride into nanosheets had an effect on the chemiresistor's photoexcitation behavior. Non-exfoliated graphitic carbon nitride/rGO chemiresistor in humid nitrogen showed a 32% increase in conductance when irradiated with UV light for five minutes (Figure S8). In comparison, exfoliated carbon nitride/rGO chemiresistor increased by 160% when irradiated with UV light for five minutes (Figure

3A). This large difference in photoexcitation between non-exfoliated and exfoliated carbon nitride can be explained by several possible effects: 1) exfoliated carbon nitride absorbs more UV light than non-exfoliated carbon nitride due to a shift in bandgap;[25] 2) exfoliation of carbon nitride into nanosheets "unstacks" carbon nitride such that there is a larger carbon nitride surface area; or 3) carbon nanosheets are able to form a better interface with rGO than non-exfoliated sheets due to their size (10-100 nm vs. 1-3 μm).

As charge transfer from UV-irradiated carbon nitride into the rGO transducer was hypothesized, the carbon nitride/rGO chemiresistor was exposed to oxygen gas in both dry and humid conditions. Oxygen is an oxidizing gas that will react with photoexcited electrons if their potential is large enough. In dry N_2 background, 5% oxygen exposures with and without UV irradiation showed little to no effect on chemiresistor's conductance (Figure 3B). Likewise, in humid N_2 background without UV irradiation, 5% oxygen exposure had little effect on the chemiresistor (Figure S9). In contrast, under humid conditions and UV light, the carbon nitride/rGO chemiresistor showed a large drop in conductance when exposed to oxygen (Figure S10). In the same experiment the conductance of the chemiresistor was found to increase once the oxygen exposure ended. A reversible response indicates that oxygen gas is not irreversibly adsorbed, but rather reacts with photoexcited electrons.

A set of 3-minute exposures of oxygen concentrations ranging from 300-100,000 parts per million by volume (ppm_v) were tested. The experimental data shown in Figure S10 is representative of the data used to form the oxygen sensor calibration curve shown in Figure 3C. The response (eq. 2) of the chemiresistor in the first minute of oxygen exposure was found to be logarithmically proportional to oxygen concentration (Figure 3C). For eq. 2, G_0 is conductance of the chemiresistor at t=0 minutes after oxygen exposure, while G_1 is conductance at t=1 minute after oxygen exposure.

$$sensor\ response = \frac{G_0 - G_1}{G_0} * 100 \qquad \text{(eq. 2)}$$

Each chip has four chemiresistor devices which allow four simultaneous sensor responses to every oxygen exposure. The limit of quantification (LOQ) for this sensor, assuming the logarithmic function (eq. 3) continues for concentrations <300 ppm, was found to be 20 ppm. LOQ was determined as the oxygen concentration that exceeds ten times the standard deviation of the blank ($10SD_{blank}$ = 0.015).

$$sensor\ response = 3.575 \ln(O_2\ \text{vol\%}) + 24.59 \qquad \text{(eq. 3)}$$

Response and recovery time of the sensor can be improved by increasing the power of the UV light source. When the UV light source was changed to a LED (4.2 mW/cm^2), the sensor's response and recovery times improved to 38 and 39 seconds, respectively, for exposure to 0.1% O_2 (Figure 3D). This result suggests that the rate of charge carrier photogeneration, which is contingent on UV light power, is directly correlated with sensor performance.

3.4 Oxygen sensing mechanism. Kofuji *et al.* studied a similar system of carbon nitride on rGO, albeit in a photoelectrochemical set-up.[39] Their results showed that photoexcited electrons are generated in carbon nitride and transferred to the rGO sheet. In their photocatalyst experiment, photogenerated holes remain on carbon nitride and oxidize water to oxygen gas, while the photogenerated electrons reduce oxygen to hydrogen peroxide on the rGO surface. The same charge separation from carbon nitride to rGO was observed in this work. It is this charge transfer to rGO that makes the chemiresistor sensitive to oxygen gas since bare rGO shows no response to O_2, whether with or without UV irradiation (Figure S11). Charge

Scheme 1. Photoredox mechanism for oxygen sensing on photoexcited carbon nitride/rGO.

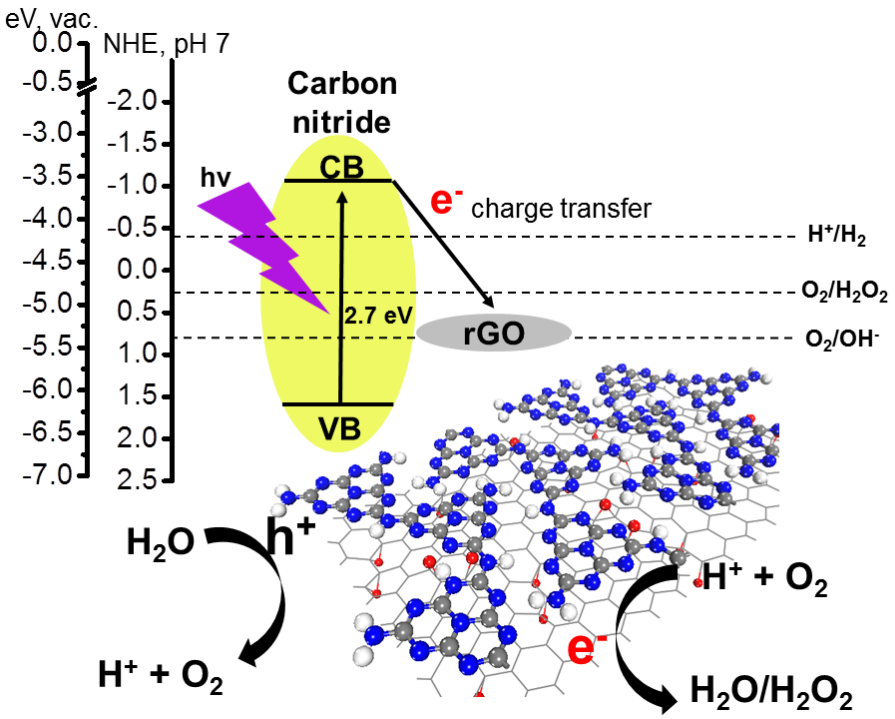

transfer from carbon nitride to rGO was evidenced by a large conductance increase of the carbon nitride/rGO chemiresistor under UV irradiation. In dry nitrogen background the conductance remains elevated even after the UV light is removed, indicating that charge recombination between photogenerated electrons and holes does not occur once the photogenerated electrons are separated in the carbon nitride/rGO system. The work functions of carbon nitride and rGO were determined by taking valence XPS spectra of each material and comparing to copper foil's valence XPS spectrum (Figure S12). Determination of carbon nitride and rGO's approximate Fermi levels allows the comparison of each material's electronic bands against a standard electrode potential (Scheme 1). Carbon nitride is a semiconductor with a ~2.7 eV bandgap while rGO is a semi-metal with little to no bandgap. Charge transfer from carbon nitride's conduction band to rGO places photoexcited electrons at a potential exceeding that of 4-e^- reduction potential of O_2. From a Koutecky-Levich plot, the calculated electron transfer number, n = 2.30, indicates a 2 e^- reduction process (Figure S19). This result is comparable to the findings of Kofuji *et al.*, who found n = 2.10 for their carbon nitride/rGO material.[39] In humid conditions, photogenerated holes on carbon nitride oxidize water to O_2. Water oxidation provides protons, thus allowing photoexcited electrons on rGO to reduce O_2 to H_2O or H_2O_2. The absence of protons in dry conditions prevents oxygen reduction, which corresponds to the lack of oxygen sensitivity in dry conditions (Figure 3B). Recovery toward baseline once UV irradiation is removed (Figures 3A, S7) can also be understood with the photoredox mechanism. In humid conditions a small concentration of O_2 is present due to water oxidation, while dry conditions are always anaerobic unless O_2 is introduced. According to the photoredox mechanism (Scheme 1), the sensor should have a response to O_2 concentrations as long as the rate of O_2 reduction exceeds the rate of charge transfer from carbon nitride to rGO. The carbon nitride/rGO chemiresistor showed little to no response to large concentrations (5 vol%) of H_2 or CO_2 (Figures S13, S14). There was a small sensor response toward H_2 gas only when the carbon nitride/rGO system was irradiated with UV light (Figure S13). Reducing gases cannot react with photogenerated electrons transferred to the rGO conduction band, but may react with the photogenerated holes remaining in the carbon nitride valence band. Oxidative splitting of H_2 gas on the carbon nitride layer would hydrogenate the carbon nitride layer and thus slow the rate of electron/hole pair photogeneration. This indirect photoredox sensing mechanism occurring on the carbon nitride layer rather than the rGO layer would explain why the sensor response toward H_2 gas is only a tenth the response toward the same concentration of O_2 gas. CO_2, on

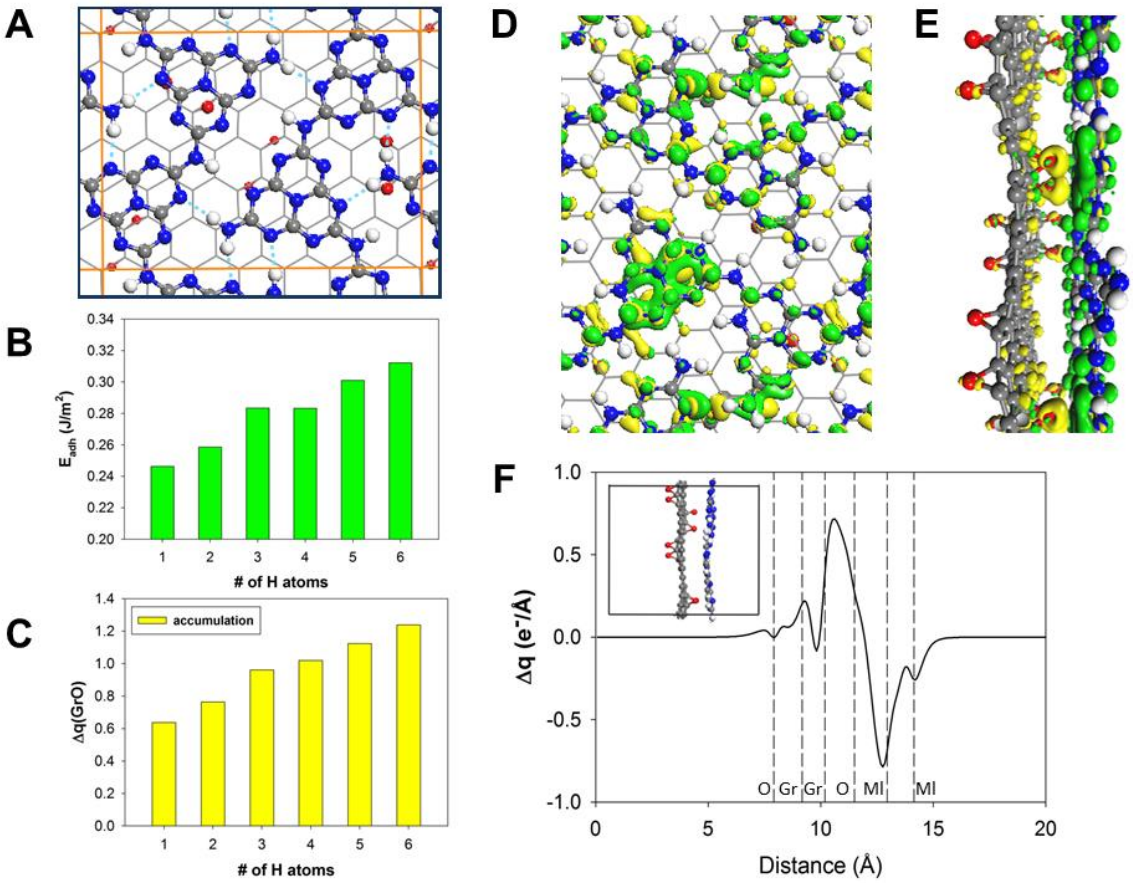

Figure 4. (A) Top view of the supercell (C gray, N blue, O red, H white). rGO oxidation, assumed to be largely due to epoxide species, are distributed in pairs on both sides of rGO sheets at a relative O/C concentration ratio of ~10%, similar to the value measured experimentally. Panel (B) indicates the variation of the adhesion energy of the melon layer and rGO with increase in the number of pyridinic H atoms on melon. (C) Variation of the Bader charges on rGO upon increase in the number of pyridinic H atoms on melon. Top (D) and side (E) views of the charge density difference maps for a protonated melon layer (ML) adsorbed on a reduced graphene oxide layer. The indicated isosurfaces correspond to values of 0.008 e/Å^3 (yellow) and -0.008 e/Å^3 (green) and show the regions of charge accumulation (on rGO) and of depletion (on melon), respectively. The charge density difference was calculated as $\Delta\rho(r) = \rho_{ML/rGO}(r)-\rho_{ML}(r)-\rho_{rGO}(r)$, where $\rho_{ML/rGO}(r)$ is the total charge density distribution of the combined ML/rGO system and $\rho_{ML}(r)$ and $\rho_{rGO}(r)$ are the total charge distributions of the isolated melon and rGO. (F) The plane averaged charge density difference plot for melon-rGO system at different z-planes (taken perpendicular to rGO layer), respectively. The labels O, Gr, and MI indicate the range of locations (in a direction perpendicular to surface) for O and for the atoms of graphene and melon layers, respectively.

the other hand, is an oxidizing gas but the reduction potential for CO_2 is much greater than the reduction potential for O_2. While the reduction potentials for O_2 fall near rGO's work function, the reduction potentials for CO_2 are much closer to H^+ reduction potential, thus making the chemiresistor unresponsive to CO_2 (Figure S14). This result shows how the photoredox sensing mechanism allows selectivity to be tuned based on the location of the transducer's Fermi level on the energy scale.

3.5 DFT calculations of carbon nitride/rGO interface. Additional insight into the properties of the melon-graphene hybrid system has been obtained through first principles density functional theory calculations. The primary objective of these investigations was to monitor the charge transfer properties at the melon-graphene interface by varying the concentration of O (epoxy) adsorbed on graphene and of H atoms adsorbed at the pyridinic sites of melon. In order to theoretically simulate these effects, we used a periodic slab model containing a graphene sheet (Figure 4A) on which a melon layer is adsorbed. Details of the geometric parameters of this model and of the computational method used to optimize and analyze the electronic properties of this hybrid system are provided in Computational Methods section.

The first set of studies is detailed in Figure S15 and corresponds to the case when a variable concentration of epoxy species is present on a graphene sheet, in the case of the composite melon/rGO system. The maximum concentration of epoxy species relative to the C (graphene) concentration was taken to be similar to the O concentration observed experimentally, namely of ~10 atomic% (Figure S16). This corresponds to a maximum number of eight epoxy species for the size of the supercell model used. The increase in concentration of the epoxy species on graphene leads to out of plane deformations of the melon and graphene layers relative to their planar structures found in the absence of O species, as well as an increase of the graphene-melon gap distance and a corresponding de-

crease in the cohesive energy (Figure S15B). The specific variations of these quantities are dependent on which side of the graphene layer the epoxy groups are, *i.e.* towards or opposite to the melon layer, and on the relative number of epoxy species on each side of graphene. A case of non-isotropic distribution with a maximum of six epoxy species in the gap versus two on the bottom graphene side (denoted as Set 2 in Figure S15A) leads to a larger decrease in the adhesion energy than the case of a distribution with equal number of epoxy species on both sides of graphene (denoted as Set 1 in Figure S15A). The increase in concentration of epoxy species also influences the amount and direction of charge transfer between the graphene and melon layers. Specifically, in the case of the bare graphene-melon system, charge transfer takes place from graphene to melon. Increasing the concentration of epoxy species leads to a systematic drop in the amount of charge transferred from graphene to melon and even to a reversal in direction of charge transfer, *i.e.* from melon to graphene, as seen in Figure S15 for the case of larger concentrations of epoxy species with a non-isotropic distribution (*i.e.* Set 2 with more species in the gap region than on the bottom surface of graphene).

The second set of investigations focused on protonation of the melon layer (Figure S17). In this case, successive protonation of melon's pyridinic sites up to six protonated pyridinic N, which is the maximum that can be accommodated by the supercell used, was studied (Figure S17). Increasing protonation of melon's pyridinic sites has an opposite effect than the one determined for epoxy species, primarily with respect to the coupling of the melon and graphene layers. Instead of a decrease in adhesion energy with increase in epoxy concentration (Figure S15B), the increase of protonated pyridines leads to enhanced attraction between melon and graphene as reflected by larger adhesion energies between these layers (Figure S17D) and a corresponding smaller graphene-melon interlayer distance (Figure S17E). Furthermore, protonation leads to charge accumulation on graphene layer and depletion from melon. This behavior can be seen in both the variation of the Bader charges of graphene layer (Figure S17F), as well as from the charge density distribution (Figure S17C). It should be noted that despite similar ranges of concentration variations for O (epoxy) and H (protonated pyridinic) species considered in these theoretical investigations, H atoms on melon lead to significantly larger variation in either adhesion energy (Figures S15B and S17D) or in the amount of charge transferred among the two layers (Figures S15C and S17F) than those induced by epoxy species.

These findings remain valid in the case of the composite system containing about 10% of epoxy species on graphene and a variable number of pyridinic H atoms on melon, ranging from 1-6 atoms (Figure 4). Consistent with observations described above, the increased concentration of pyridinic H leads to an increased adhesion of rGO and melon layers (Figure 4B) and an increasingly larger charge transfer from melon to graphene (Figure 4C). Charge is seen to accumulate primarily in the gap region, just above the graphene surface as shown by the plane averaged charge density difference plot given in Figure 4F and also visualized by the charge difference plots in Figures 4D and 4E. Experimentally, the as-synthesized carbon nitride material was found to have 2 protonated pyridinic N per unit cell. According to the calculated effect of 2 H atoms on pyridinic N sites, the adhesion energy between the melon and rGO layer does not vary greatly between 0 and 2 H atoms (0.22 J/m^2 vs. 0.26 J/m^2, respectively). However, protonation of the melon layer has a large effect on the direction and magnitude of charge transfer between the two layers. Melon with two protonated pyrdinic N sites layered on rGO shows charge accumulation on the rGO layer (0.8 e^-), while melon with no protonation layered on rGO shows a slight charge depletion on the rGO layer (-0.01 e^-). Overall, these findings point to the important role provided by pyridinic H atoms to modulate both the interaction between the melon and rGO layers and the amount and direction of charge transferred among these two systems.

4.0 CONCLUSIONS

In this work, it was shown that uncondensed graphitic carbon nitride (melon) coupled to rGO can sense oxygen gas within the concentration range of 300-10,000 ppm. Through XRD, fluorescence spectroscopy, and XPS characterization it was determined that the as-synthesized carbon nitride material was heptazine-based uncondensed graphitic carbon nitride (gh-$C_6N_9H_3$). XPS characterization, especially N_{1s} XPS, provided structural insight into the degree of sp^2 N protonation on the synthesized carbon nitride. The N_{1s} peak centered at 403.8 eV was found to be correlated with positive charge localization caused by protonation of pyridinic N sites. The as-synthesized carbon nitride material was exfoliated into nanosheets *via* bath sonication, which proved to have an advantageous effect toward sensing application. Carbon nitride/rGO chemiresistor devices were prepared and tested for oxygen sensitivity in humid and dry conditions with and without UV irradiation. UV irradiation doubled the measured conductance of the carbon nitride/rGO chemiresistor due to charge transfer of photoexcited electrons from carbon nitride nanosheets to the rGO transducer. The carbon nitride/rGO chemiresistor significantly dropped in conductance whenever exposed to oxygen gas in humid conditions and under UV irradiation. A photoredox mechanism wherein water is oxidized on the carbon nitride surface and oxygen is reduced on the rGO surface explains the chemiresistor behavior observed. The chemiresistor's response to oxygen was found to be logarithmically proportional to oxygen concentration in the range 300-10,000 ppm. DFT calculations were carried out on a melon-oxidized graphene system in order to understand the charge transfer effects at the interface between the carbon nitride nanosheets and rGO observed in experiments. The level of oxidation on the graphene layer in rGO relevant concentrations was found to have a small effect on adhesion energy and charge distribution between the two layers. Protonation of the pyridinic groups on the melon layer, however, was found to increase the adhesion energy between the two layers, thus decreasing the interlayer distance. Importantly, protonation of the melon layer was found to dramatically affect the charge transfer between the two layers such that charge accumulation occurred on the rGO layer. The direction of charge transfer determined through DFT calculations agreed with our experimental observation that photoexcited electrons rather than holes are transferred to the rGO sheet. A close electrical interface between two materials like the one observed in this work is a crucial feature for sensing, photocatalysis, and photovoltaic applications.

2. EXPERIMENTAL SECTION

2.1 Synthesis and Preparation of Exfoliated "Graphitic" Carbon Nitride.

Dicyandiamide (DCDA, 99% purity, 1 gram; Sigma-Aldrich) was placed in an open quartz boat, which was subsequently placed in a quartz tube. The quartz tube atmosphere was replaced with argon and the tube was sealed on both ends by water bubblers. The sample was heated in a CVD furnace (Lindberg blue 3-zone furnace) for 2 hours at 550ºC and left to cool

overnight. The remaining pale-yellow solid (~140 mg) was recovered from the quartz boat and ground in a mortar and pestle for ~10 minutes to yield a fine powder. In order to exfoliate the bulk sheets into nanosheets, the resultant carbon nitride powder was dispersed in nanopure water (100 μg/mL) and sonicated in a bath sonicator (Branson 1510) for 1 hour.

2.2 Preparation of rGO/Carbon Nitride Chemiresistor Devices.

rGO was prepared through a previously described chemical reduction method.[53] Briefly, graphene oxide (5 mL, 3 mg/mL in H_2O; Graphene Supermarket) was stirred with 5 μL of hydrazine hydrate (ca. 51% hydrazine; Acros Organics) in an 80 ºC oil bath for 3 hours. The black precipitate (rGO) was collected through vacuum filtration and dispersed in DMF. Si chips, each containing 4 devices with interdigitated Au electrodes, were fabricated in-house and connected to 40 CERDIP packages with Au wires. 3 μL of rGO (0.1 mg/mL in DMF) is dropped above the chip and, *via* dielectrophoresis (DEP; 10 V_{pp}, 300 kHZ, 10 seconds), rGO sheets were deposited between the interdigitated electrodes. Exfoliated carbon nitride was deposited above rGO on the devices by dropcasting 3 μL of exfoliated carbon nitride (0.1 mg/mL in H_2O) on top of the chip and evaporating off the solvent by placing the packaged chip on a 130ºC hotplate. Thickness of the carbon nitride layer above rGO can be controlled by the volume of solution dropcast, as well as the concentration of the solution.

2.3 **Oxygen Sensing Experiment Set-up**.

Packaged rGO/carbon nitride chemiresistor chips were placed on a test board and sealed in a Teflon chamber. The test board was connected to a Keithley Dual SourceMeter 2602 and Keithley Switching Matrix 708A, which were controlled with Labview software. This set-up extracts 4 data outputs simultaneously, allowing changes in electrical conductance of each chemiresistor device to be collected with Zephyr data-acquisition software (http://zephyr.sourceforge.net). Two gas flow controllers were used to control the concentration of oxygen in the Teflon test chamber. The diluting gas flow controller was connected to dry N_2 and the experimental gas flow controller was connected to dry air (for concentrations 1-5% O_2) or 1% O_2 in dry N_2 (for concentrations 0.05-0.5% O_2). In order to humidify the gas, a glass-fritted water bubbler filled with DI H_2O was connected in-line before the Teflon chamber, thus delivering 100% relative humidity at 21 ºC. The gas velocity was kept at 540 standard cubic centimeters per minute (sccm) for all experiments. The bias voltage for all experiments was 50 mV. For the sensing experiments that provided the calibration curve data, UV light was provided by a handheld lamp (Analytik Jena (UVP) UVGL-55). The longwave (365 nm) source was used at a distance of three inches, thus providing 950 μW/cm^2. In order to demonstrate the effect UV light power on the sensor performance, a longwave UV LED (LED Engin LZ1-10UA00-00U4, 385-390 nm) was used that provided an irradiance of 4.2 mW/cm^2.

ASSOCIATED CONTENT

Supporting Information. Characterization and computational methods; XPS data of carbon nitride; TEM of exfoliated carbon nitride; XPS and TEM of bare rGO; control gas sensing experiments; LSV and K-L plots of carbon nitride/rGO composite; DFT computational studies of rGO oxidation and carbon nitride protonation effects on carbon nitride/rGO composite material. This supporting information is available free of charge at pubs.acs.org.

AUTHOR INFORMATION

Corresponding Author

* Address correspondence to astar@pitt.edu

Notes

The authors declare no competing financial interest.

ACKNOWLEDGMENT

This work was partially supported by the National Institutes of Health through Grant Number 5UL1TR000005-09. We thank the Department of Biological Sciences and the Nanoscale Fabrication and Characterization Facility at the University of Pittsburgh for access to the TEM, SEM, and XRD instrumentation. We also thank Dr. Damodaran Achary of the University of Pittsburgh, Department of Chemistry NMR facility for collecting the solid-state NMR spectra and David White for his help with graphic preparation.

ABBREVIATIONS

rGO, reduced graphene oxide; ML, protonated melon layer.

REFERENCES

1. G. Muller, G. Krotz, J. Schalk. New Sensors for Automotive and Aerospace Applications, *Phys. Stat. Sol. (a)* **2001**, *185*, 1-14
2. N. Docquier, S. Candel. Combustion Control and Sensors: A Review, *Prog. Energy Combustion Sci.* **2002**, *28*, 107-150
3. E. Ikeda. Cellular Response to Tissue Hypoxia and Its Involvment in Disease Progression, *Pathol. Int.* **2005**, *55*, 603-610
4. A. L. Harris. Hypoxia-a Key Regulatory Factor in Tumour Growth, *Nat. Rev. Cancer* **2002**, *2*, 38-47
5. C. Wu, B. Bull, K. Christensen, J. McNeill. Ratiometric Single-Nanoparticle Oxygen Sensors for Biological Imaging, *Angew. Chem. Int. Ed.* **2009**, *48*, 2741-2745
6. M. E. Franke, T. J. Koplin, U. Simon. Metal and Metal Oxide Nanoparticles in Chemiresistors: Does the Nanoscale Matter?, *Small* **2006**, *2*, 36-50
7. D. R. Kauffman, C. M. Shade, H. Uh, S. Petoud, A. Star. Decorated Carbon Nanotubes with Unique Oxygen Sensitivity, *Nat. Chem.* **2009**, *1*, 500-506
8. T. Wang, D. Huang, Z. Yang, S. Xu, G. He, X. Li, N. Hu, G. Yin, D. He, L. Zhang. A Review on Graphene-Based Gas/Vapor Sensors with Unique Properties and Potential Application, *Nano-Micro Lett.* **2016**, *8*, 95
9. J. E. Ellis, A. Star. Carbon Nanotube Based Gas Sensors Toward Breath Analysis, *ChemPlusChem* **2016**, *81*, 1248-1265
10. W. Yuan, G. Shi. Graphene-Based Gas Sensors, *J. Mater. Chem. A* **2013**, *1*, 10078-10091
11. M. Meyyappan. Carbon Nanotube-Based Chemical Sensors, *Small* **2016**, *12*, 2118-2129
12. M. Ding, Y. Tang, A. Star. Understanding Interfaces in Metal-Graphitic Hybrid Nanostructures, *J. Phys. Chem. Lett.* **2013**, *4*, 147-160
13. A. Kudo, Y. Miseki. Heterogeneous Photocatalyst Materials for Water Splitting, *Chem. Soc. Rev.* **2009**, *38*, 253-278
14. Y. Qu, X. Duan. Progress, Challenge and Perspective of Heterogeneous Photocatalysts, *Chem. Soc. Rev.* **2013**, *42*, 2568-2580
15. A. Thomas, A. Fischer, F. Goettmann, M. Antonietti, J.-O. Muller, R. Schlogl, J. M. Carlsson. Graphitic Carbon Nitride Materials: Variation of Structure and Morphology and Their Use as Metal-Free Catalysts, *J. Mater. Chem.* **2008**, *18*, 4893-4908
16. Y. Wang, X. Wang, M. Antonietti. Polymeric Graphitic Carbon Nitride as a Heterogeneous Organocatalyst: From Photochemistry to Multipurpose Catalysis to Sustainable Chemistry, *Angew. Chem. Int. Ed.* **2012**, *51*, 68-89
17. Y. Zheng, L. Lin, B. Wang, X. Wang. Graphitic Carbon Nitride Polymers toward Sustainable Photoredox Catalysis, *Angew. Chem. Int. Ed.* **2015**, *54*, 12868-12884

18. X. Wang, K. Maeda, A. Thomas, K. Takanabe, G. Xin, J. M. Carlsson, K. Domen, M. Antonietti. A Metal-Free Polymeric Photocatalyst for Hydrogen Production from Water Under Visible Light, *Nat. Mater.* **2009**, *8*, 76-80
19. P. Niu, L. Zhang, G. Liu, H.-M. Cheng. Graphene-Like Carbon Nitride Nanosheets for Improved Photocatalytic Activities, *Adv. Funct. Mater.* **2012**, *22*, 4763-4770
20. Y. Cui, Z. Ding, P. Liu, M. Antonietti, X. Fu, X. Wang. Metal-Free Activation of H_2O_2 by g-C_3N_4 Under Visible Light Irradiation for the Degradation of Organic Pollutants, *Phys. Chem. Chem. Phys.* **2012**, *14*, 1455-1462
21. S. Yang, X. Feng, X. Wang, K. Mullen. Graphene-Based Carbon Nitride Nanosheets as Efficient Metal-Free Electrocatalysts for Oxygen Reduction Reactions, *Angew. Chem. Int. Ed.* **2011**, *50*, 5339-5343
22. Y. Zheng, Y. Jiao, J. Chen, J. Liu, J. Liang, A. Du, W. Zhang, Z. Zhu, S. C. Smith, M. Jaroniec, G. Q. Lu, S. Z. Qiao. Nanoporous Graphitic-C_3N_4@Carbon Metal-Free Electrocatalysts for Highly Efficient Oxygen Reduction, *J. Am. Chem. Soc.* **2011**, *133*, 20116-20119
23. Y. Kofuji, S. Ohkita, Y. Shiraishi, H. Sakamoto, S. Tanaka, S. Ichikawa, T. Hirai. Graphitic Carbon Nitride Doped with Biphenyl Diimide: Efficient Photocatalysts for Hydrogen Peroxide Production from Water and Molecular Oxygen by Sunlight, *ACS Catal.* **2016**, *6*, 7201-7029
24. Y. Li, S. Ouyang, H. Xu, X. Wang, Y. Bi, Y. Zhang, J. Ye. Constructing Solid-Gas-Interfacial Fenton Reaction over Alkanized-C_3N_4 Photocatalyst to Achieve Apparent Quantum Yield of 49% at 420 nm, *J. Am. Chem. Soc.* **2016**, *138*, 13289-13297
25. P. Niu, Y. Yang, J. C. Yu, G. Liu, H.-M. Cheng. Switching the Selectivity of the Photoreduction Reaction of Carbon Dioxide by Controlling the Band Structure of a g-C_3N_4 Photocatalyst, *Chem. Commun.* **2014**, *50*, 10837-10840
26. G. Gao, Y. Jiao, E. R. Waclawik, A. Du. Single Atom (Pd/Pt) Supported on Graphitic Carbon Nitride as an Efficient Photocatalyst for Visible-Light Reduction of Carbon Dioxide, *J. Am. Chem. Soc.* **2016**, *138*, 6292-6297
27. J. Gracia, P. Kroll. Corrugated Layered Heptazine-Based Carbon Nitride: the Lowest Energy Modifications of C_3N_4 Ground State, *J. Mater. Chem.* **2009**, *19*, 3013-3019
28. G. Algara-Siller, N. Severin, S. Y. Chong, T. Bjorkman, R. G. Palgrave, A. Laybourn, M. Antonietti, Y. Z. Khimyak, A. V. Krasheninnikov, J. P. Rabe, U. Kaiser, A. I. Cooper, A. Thomas, M. J. Bojdys. Triazine-Based Graphitic Carbon Nitride: a Two-Dimensional Semiconductor, *Angew. Chem. Int. Ed.* **2014**, *53*, 7450-7455
29. C. E. Redemann, H. J. Lucas. Some Derivatives of Cyameluric Acid and Probable Structures of Melam, Melem and Melon, *J. Am. Chem. Soc.* **1940**, *62*, 842-846
30. B. V. Lotsch, M. Doblinger, J. Sehnert, L. Seyfarth, J. Senker, O. Oeckler, W. Schnick. Unmasking Melon by a Complementary Aproach Employing Electron Diffraction, Solid-State NMR Spectroscopy, and Theoretical Calculations-Structural Characterization of a Carbon Nitride Polymer, *Chem. Eur. J.* **2007**, *13*, 4969-4980
31. W. Wang, J. C. Yu, Z. Shen, D. K. L. Chan, T. Gu. g-C_3N_4 Quantum Dots: Direct Synthesis, Upconversion Properties and Photocatalytic Application, *Chem. Commun.* **2014**, *50*, 10148-10150
32. F. K. Kessler, Y. Zheng, D. Schwarz, C. Merschjann, W. Schnick, X. Wang, M. J. Boyjdys. Functional Carbon Nitride Materials -- Design Strategies for Electrochemical Devices, *Nat. Rev. Mater.* **2017**, *2*, 17030
33. J. Duan, S. Chen, M. Jaroniec, S. Z. Qiao. Porous C_3N_4 Nanolayers@N-Graphene Films as Catalyst Electrodes for Highly Efficient Hydrogen Evolution, *ACS Nano* **2015**, *9*, 931-940
34. Q. Xiang, J. Yu, M. Jaroniec. Preparation and Enhanced Visible-Light Photocatalytic H_2-Production Activivty of Graphene/C_3N_4 Composites, *J. Phys. Chem. C* **2011**, *115*, 7355-7363
35. Q. Liu, J. Zhang. Graphene Supported Co-g-C_3N_4 as a Novel Metal-Macrocyclic Electrocatalyst for the Oxygen Reduction Reaction in Fuel Cells, *Langmuir* **2013**, *29*, 3821-3828
36. T. Y. Ma, S. Dai, M. Jaroniec, S. Z. Qiao. Graphitic Carbon Nitride Nanosheet-Carbon Nanotube Three-Dimensional Porous Composites as High-Performance Oxygen Evolution Electrocatalysts, *Angew. Chem. Int. Ed.* **2014**, *53*, 7281-7285
37. Y. Li, H. Zhang, P. Liu, D. Wang, Y. Li, H. Zhao. Cross-Linked g-C_3N_4/rGO Nanocomposites with Tunable Band Structure and Enhanced Visible Light Photocatalytic Activity, *Small* **2013**, *9*, 3336-3344
38. K. Chen, Z. Chai, C. Li, L. Shi, M. Liu, Q. Xie, Y. Zhang, D. Xu, A. Manivannan, Z. Liu. Catalyst-Free Growth of Three-Dimensional Graphene Flakes and Graphene/g-C_3N_4 Composite for Hydrocarbon Oxidation, *ACS Nano* **2016**, *10*, 3665-3673
39. Y. Kofuji, Y. Isobe, Y. Shiraishi, H. Sakamoto, S. Tanaka, S. Ichikawa, T. Hirai. Carbon Nitride-Aromatic Diimide-Graphene Nanohybrids: Metal-Free Photocatalysts for Solar-to-Hydrogen Peroxide Energy Conversion with 0.2% Efficiency, *J. Am. Chem. Soc.* **2016**, *138*, 10019-10025
40. E. Wirnhier, M. Doblinger, D. Gunzelmann, J. Senker, B. V. Lotsch, W. Schnick. Poly(triazine imide) with Intercalation of Lithium and Chloride Ions $[(C_3N_3)_2(NH_xLi_{1-x})_3$-LiCl]: A Crystalline 2D Carbon Nitride Network, *Chem. Eur. J.* **2011**, *17*, 3213-3221
41. S. Zuluaga, L.-H. Liu, N. Shafig, S. M. Rupich, J.-F. Veyan, Y. J. Chabal, T. Thonhauser. Structural Band-Gap Tuning in g-C_3N_4, *Phys. Chem. Chem. Phys.* **2015**, *17*, 957-962
42. P. Niu, L.-C. Yin, Y.-Q. Yang, G. Liu, H.-M. Cheng. Increasing the Visible Light Absorption of Graphitic Carbon Nitride (Melon) Photocatalysts by Homogenous Self-Modification with Nitrogen Vacancies, *Adv. Mater.* **2014**, *26*, 8046-8052
43. R. J. J. Jansen, H. v. Bekkum. XPS of Nitrogen-Containing Functional Groups on Activated Carbon, *Carbon* **1995**, *33*, 1021-1207
44. J. R. Pels, F. Kapteijn, J. A. Moulijn, Q. Zhu, K. M. Thomas. Evolution of Nitrogen Functionalities in Carbonaceous Materials during Pyrolysis, *Carbon* **1995**, *33*, 1641-1653
45. M. A. Wojtowicz, J. R. Pels, J. A. Moulijn. The Fate of Nitrogen Functionalities in Coal during Pyrolysis and Combustion, *Fuel* **1995**, *74*, 507-516
46. S. Yang, Y. Gong, J. Zhang, L. Zhan, L. Ma, Z. Fang, R. Vajtai, X. Wang, P. M. Ajayan. Exfoliated Graphitic Carbon Nitride Nanosheets as Efficient Catalysts for Hydrogen Evolution Under Visible Light, *Adv. Mater.* **2013**, *25*, 2452-2456
47. W.-J. Ong, L. K. Putri, Y.-C. Tan, L.-L. Tan, N. Li, Y. H. Ng, X. Wen, S.-P. Chai. Unravelling Charge Carrier Dynamics in Protonated g-C_3N_4 Interfaced with Carbon Nanodots as Co-Catalysts toward Enhanced Photocatalytic CO_2 Reduction: A Combined Experimental and First-Principles DFT Study, *Nano Res.* **2017**, *Advance online publication*, DOI 10.1007/s12274-016-1391-4
48. C. Gomez-Navarro, J. C. Meyer, R. S. Sundaram, A. Chuvilin, S. Kurasch, M. Burghard, K. Kern, U. Kaiser. Atomic Structure of Reduced Graphene Oxide, *Nano Lett.* **2010**, *10*, 1144-1148
49. S. U. Yu, B. Park, Y. Cho, S. Hyun, J. K. Kim, K. S. Kim. Simultaneous Visualization of Graphene Grain Boundaries and Wrinkles with Structural Information by Gold Deposition, *ACS Nano* **2014**, *8*, 8662-8668
50. W.-J. Ong, L.-L. Tan, S.-P. Chai, S.-T. Yong, A. R. Mohamed. Surface Charge Modification via Protonation of Graphitic Carbon Nitride (g-C_3N_4) for Electrostatic Self-Assembly Construction of 2D/2D Reduced Graphene Oxide (rGO)/g-C_3N_4 Nanostructures toward Enhanced Photocatalytic Reduction of Carbon Dioxide to Methane, *Nano Energy* **2015**, *13*, 757-770

51. G. Chen, T. M. Paronyan, A. R. Harutyunyan. Sub-ppt Gas Detection with Pristine Graphene, *Appl. Phys. Lett.* **2012**, *101*, 053119
52. X. Lu, K. Xu, P. Chen, K. Jia, S. Liu, C. Wu. Facile One Step Method Realizing Scalable Production of g-C_3N_4 Nanosheets and Study of Their Photocatalytic H_2 Evolution Activity, *J. Mater. Chem. A* **2014**, *2*, 18924-18928
53. S. Park, J. An, J. R. Potts, A. Velamakanni, S. Murali, R. S. Ruoff. Hydrazine-Redution of Graphite- and Graphene Oxide, *Carbon* **2011**, *49*, 3019-3023

TOC image